Electronic structure and polaronic charge distributions of Fe vacancy clusters in $Fe_{1-x}O$

I. Bernal-Villamil and S. Gallego*

Instituto de Ciencia de Materiales de Madrid, Consejo Superior de Investigaciones Científicas, Cantoblanco, 28049 Madrid, Spain

(Received 6 August 2014; revised manuscript received 24 October 2014; published 17 November 2014)

We perform a detailed study of the electronic structure of $Fe_{1-x}O$ at moderate values of x. Our results evidence that the Fe vacancies introduce significant local modifications of the structural, electronic, and magnetic features, which serve to explain the origin of the measured dependencies of the physical properties on x. The final properties are determined by a complex interplay of the charge demand from O, the magnetic interactions, and the charge order at the Fe sublattice. Furthermore, polaronic distributions of charge resembling those at magnetite, Fe_3O_4, emerge for the most stable defect structures. This defines a unique scenario to understand the nature of the short-range correlations in Fe_3O_4, and unveils their intimate connection to the long-range charge order developed below the Verwey transition temperature.

DOI: 10.1103/PhysRevB.90.195126 PACS number(s): 75.25.Dk, 61.72.−y, 71.20.−b, 91.60.Ed

I. INTRODUCTION

FeO belongs to the magnetic transition metal monoxides (TMO) series, together with MnO, CoO, and NiO. They share similar properties, such as a cubic NaCl crystal lattice, large insulating gaps, or antiferromagnetism of AF-II type, where adjacent ferromagnetic (111) cation planes couple antiferromagnetically. In spite of their apparent simplicity, the TMO exhibit intricate electronic interactions, and have been considered as prototypes to explore electronic correlations in the verge between Mott-Hubbard and charge transfer insulators [1]. This has motivated a large number of calculations of their properties within *ab initio* frameworks [2–5]. Furthermore, all of them show a distortion of the cubic symmetry below the Néel temperature (T_N) [6,7], which has been unequivocally related to the magnetic exchange coupling constants [8]. In the particular case of FeO, the distortion is rhombohedral, and consists in a slight elongation along the [111] direction [9]. The local magnetic moments align parallel to this direction [10], though a weak perpendicular component compatible with a departure from collinear spin order has been solved [11,12].

Within the TMO series, FeO is singular in that it shows a large deficiency in Fe ranging from 5–15% ($Fe_{1-x}O$, with $x = 0.05$–0.15) at ambient conditions. The stoichiometric form is stable at the extreme pressures and temperatures of the Earth's lower mantle, one of whose major constituents are solid solutions of the mineral form of FeO, wüstite. In fact, FeO is under scrutiny in the fields of geophysics and paleomagnetism, where large efforts are devoted to understand its complex transitions at high pressures and to determine the distribution of Fe vacancies (V_{Fe}) in the lattice [13–15]. Though unstable FeO decomposes in Fe_3O_4 and Fe below 570 °C, at room temperature the reaction is slow [6], allowing to prepare $Fe_{1-x}O$ by rapid quenching. The exact composition and local order of the defects is determined in a complex way, both by the preparation conditions and the history of the sample, and furthermore, may evolve with time [15]. However, it has been possible to identify trends revealing the influence of V_{Fe} on the physical properties of $Fe_{1-x}O$. For example, an empirical linear relation between the unit cell parameter a and x has been determined [16,17]. The magnetically induced rhombohedral distortion is also known to decrease as the Fe content decreases [6,11], and similarly the value of T_N and the specific heat anomaly at the transition depend on x [18]. The modification of the heat capacity across T_N evidences changes in the nature of the magnetic transition, with a much stronger cooperative character in FeO than in nonstoichiometric samples [11]. Also the conductivity and cation self-diffusion have been observed to depend on x, and the carrier type changes from p to n for $x \sim 0.08$ [19].

These dependencies and the high values of x admitted by wüstite suggest that Fe vacancies arrange forming specific defect structures. Their identification has been a very active field of research since the pioneering neutron diffraction study of Roth [20], and though it must be ultimately admitted that different local structures and long-range orders may exist depending on the history of a sample [15], it seems clear that there is a relation between the V_{Fe} and the emergence of interstitial Fe^{3+} cations [21,22]. Simple charge compensating arguments propose that creating an iron vacancy generates two octahedral Fe^{3+}, as has been proved from first-principles calculations of isolated V_{Fe} [23]. However, both diffraction experiments and atomistic calculations agree that the minimal defect cluster is formed by four V_{Fe} surrounding a tetrahedral Fe^{3+}, the so-called 4:1 cluster [24,25] (see Fig. 1). The aggregation of these minimal units as x increases may proceed in several ways, by face, edge, or corner sharing of neighboring 4:1 clusters. Though it is believed that the ratio between V_{Fe} and interstitials increases with temperature and at lower defect concentrations [22], different types of aggregates may coexist [26], and it is not even clear if spinel-type local structures are favored over more compact aggregations [27].

Understanding the fundamental properties of defective $Fe_{1-x}O$ at the atomic scale seems essential to determine the origin of the observed dependencies of the physical properties on x. Surprisingly, however, detailed studies of the influence of V_{Fe} on the electronic structure are scarce, and to the best of our knowledge, only isolated vacancies have been considered with *ab initio* methods [23]. Here, we perform first-principles calculations of $Fe_{1-x}O$ to determine the stability and electronic properties of 4:1 clusters, comparing them to those of isolated V_{Fe} and stoichiometric FeO. Furthermore, as the 4:1 cluster

*sgallego@icmm.csic.es

 ©2014 American Physical Society

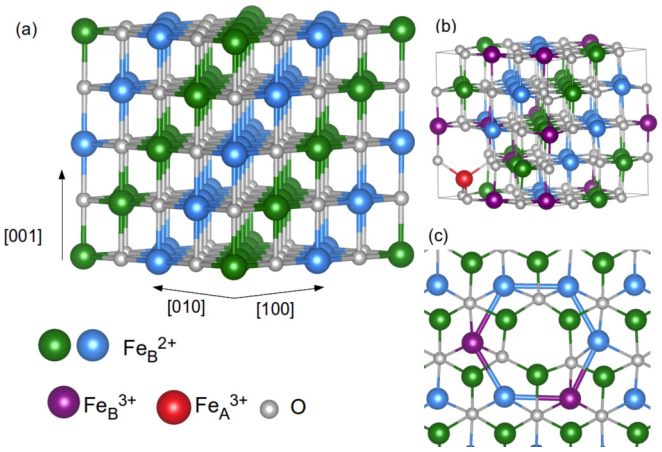

FIG. 1. (Color online) (a) Cubic unit cell of 64 atoms used to model FeO. Fe sites with opposite spin orientation are coloured in blue and green. (b) Same for a supercell with a 4:1 cluster. (c) Top view of three (111) planes around an Fe vacancy in $Fe_{0.97}O$. The central thick hexagon joins the Fe atoms surrounding the vacancy site in the blue layer.

is a basic unit for the development of spinel structures at the FeO lattice, our study provides a bridge to explore the evolution from $Fe_{1-x}O$ to Fe_3O_4, and the influence of the lattice symmetry on the local order. As we will show, this allows to extract interesting conclusions about the nature of short-range charge correlations in Fe_3O_4.

The paper is organized as follows. After describing the methodology, we provide our results for the electronic properties of FeO and isolated Fe vacancies in $Fe_{0.97}O$. Then, we describe unit cells with three V_{Fe}, corresponding to a composition $Fe_{0.906}O$, comparing two different situations: disperse V_{Fe} and 4:1 clusters. In the last section we explore the similitudes between the charge distributions of $Fe_{1-x}O$ and Fe_3O_4 based on our previous calculations of magnetite [28].

II. COMPUTATIONAL METHOD

We have performed *ab initio* calculations within density functional theory (DFT) as implemented in the VASP code [29,30], using the projector-augmented wave (PAW) method for the treatment of the core electrons [31,32] and the Perdew-Burke-Ernzerhof parametrization of the generalized gradient approximation modified for solids (PBEsol) for the exchange-correlation functional [33]. A kinetic energy cutoff of 400 eV has been used, and all symmetrizations have been removed. To take into account the important electronic correlations in Fe oxides, we have included an on-site Coulomb repulsion term U following the Dudarev approach [34]. Our choice of an effective $U - J = 4$ eV is based on the recovery of the experimental values of both the equilibrium NaCl lattice parameter ($a = 4.30$ Å) and the insulating gap ($E_g = 2.0$ eV) for stoichiometric FeO, while preserving the overlap and orbital order of the oxygen p band and the cation d states [5,35]. A similar procedure applied to Fe_3O_4 led us to the same choice of U in a previous study [36], which eases comparison of the results corresponding to both materials.

Stoichiometric FeO can be modeled with a minimal unit cell of four atoms under AF-II order. Here we have used a larger cubic unit cell of 64 atoms that allows to consider isolated 4:1 clusters as well as up to three separated V_{Fe}. A sketch of the cubic unit cell is represented in the left panel of Fig. 1, where blue and green layers denote Fe atoms with opposite spin orientation. Full relaxation of the lattice vectors and atomic positions has been performed until the forces on all atoms were lower than 0.01 eV/Å. The Brillouin zone (BZ) has been sampled using the Monhorst-Pack method, with partitions of $2 \times 2 \times 2$ during relaxations and $4 \times 4 \times 4$ for static calculations. This scheme guarantees a convergence in the total energy of 1 meV/atom. When modeling FeO with the reduced cell of four atoms, a sampling of the BZ of $7 \times 7 \times 7$ has been used.

The energy cost of creating a defect has been estimated as [37,38]:

$$E_c = E[Fe_{1-x}O] - E[FeO] + n\mu_{Fe}, \quad (1)$$

where E refers to the total energy of the supercell with ($Fe_{1-x}O$) or without (FeO) defects, n to the number of V_{Fe} introduced in the supercell, and μ_{Fe} to the chemical potential of Fe. The limits of μ_{Fe} have been obtained from calculations of the total energy of bcc Fe and the O_2 molecule, taking into account the relation between the Gibbs free energies of formation of the oxide and the stable forms of its elemental constituents, and the influence of U [39]. This allows to express E_c as a function of the O chemical potential μ_O, where we have set the zero reference state to $\mu_O = 1/2E[O_2]$.

III. STOICHIOMETRIC FeO

As mentioned in the Introduction, the electronic structure of FeO has been widely studied previously under diverse approaches, and the system has been often used as a test bed for models aiming to capture correlation effects [5,40]. Our description of stoichiometric FeO using the reduced unit cell of four atoms is in excellent agreement with previous calculations. When the large cube of 64 atoms is employed, the global features of the ground state do not vary, leading to an identical value of the cubic lattice parameter $a = 4.30$ Å, similar electronic properties, and an AF-II order of the local Fe magnetic moments (3.7 μ_B) that induces a comparable rhombohedral distortion. However, under the reduced symmetry of this large unit cell a significant deformation of the O fcc sublattice manifests, enhancing the dispersion of the atomically resolved properties, such as local charges and interatomic distances. The structural deformation already exists in the minimum unit cell of four atoms, though there it does not alter the symmetrical distribution of the Bader charges. The situation is reminiscent to that occurring in magnetite, as a hint of the close relation between the properties of both Fe oxides. The distortion of the O sublattice lowers the total energy by 21 meV/f.u., and is related to the onset of magnetism: it does not emerge in a nonmagnetic calculation, where also the elongation along [111] is lost.

The total density of states (DOS) of the supercell and its projection on the Fe atoms are in Fig. 2. Although our description of FeO corresponds to a Mott insulator, there is a strong hybridization between O and Fe states throughout the

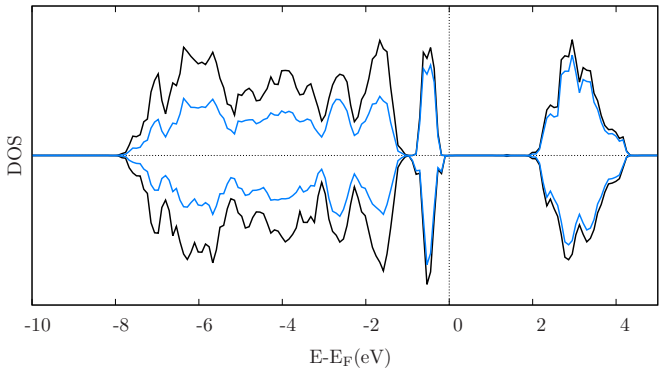

FIG. 2. (Color online) Spin-resolved DOS of stoichiometric FeO with positive (negative) values corresponding to majority (minority) spins. The black curve corresponds to the total DOS of the supercell, the blue one to the Fe contribution.

valence band (VB), with a non-negligible contribution of O at the VB edge. The orbital projection on the Fe sites shows the expected separation between t_{2g} and e_g states linked to the local octahedral coordination. Minor variations in the DOS are found at different sites, as a consequence of the asymmetry in the O sublattice, but the dispersion of the local charges is moderate, as evidenced in Table I. The first column of the table provides the mean values and the corresponding dispersions of the Bader charge (Q_B) and magnetic moment of O and Fe. Fe atoms are labeled as $Fe_B{}^{2+}$ by analogy to Fe_3O_4, as justified in the next section. The ionic nature of the Fe-O bonds manifests in the large charge transfer from Fe to O. On the other hand, the perfect compensation of the Fe magnetic moments with opposite orientations, already reflected in the DOS, leads to the negligible magnetization at the O sites.

The structural properties are summarized in Tables II and III, and Fig. 3. The rhombohedral distortion induced by the AF order stretches the cubic cell along the [111] axis perpendicular to the ferromagnetic (FM) Fe sheets, that we define as the c direction. A measure of this distortion is provided by the ratio of the mean interatomic distances between Fe neighbors at the same FM layer ($d_\parallel$) and at adjacent layers ($d_\perp$), shown in the first column of Table II. It is also evidenced from the more detailed distribution of values of $d_\parallel$ and $d_\perp$ in Fig. 3, peaked to lower values for

TABLE I. Mean values and dispersions of the Bader charges (Q_B) and magnetic moments (m) for all distinct atomic sites at the different structures under study (see text for details).

Q_B	FeO	$Fe_{0.97}O$	3 V_{Fe}	4:1
$Fe_B{}^{2+}$	6.74 ± 0.04	6.74 ± 0.04	6.72 ± 0.03	6.71 ± 0.03
$Fe_B{}^{3+}$		6.43 ± 0.02	6.39 ± 0.02	6.43 ± 0.03
$Fe_A{}^{3+}$				6.37 ± 0.00
O	7.26 ± 0.03	7.24 ± 0.05	7.22 ± 0.04	7.23 ± 0.04
$m(\mu_B)$	FeO	$Fe_{0.97}O$	3 V_{Fe}	4:1
$Fe_B{}^{2+}$	3.67 ± 0.00	3.67 ± 0.02	3.67 ± 0.02	3.68 ± 0.03
$Fe_B{}^{3+}$		4.14 ± 0.00	4.15 ± 0.02	4.14 ± 0.03
$Fe_A{}^{3+}$				4.12 ± 0.00
O	0.01 ± 0.01	0.03 ± 0.02	0.05 ± 0.04	0.05 ± 0.04

TABLE II. Mean values and dispersions of the in-plane ($d_\parallel$) and interlayer ($d_\perp$) interatomic Fe-Fe distances corresponding to (111) planes, for the structures in Table I.

d(Fe-Fe), Å	FeO	$Fe_{0.97}O$	3 V_{Fe}	4:1
$d_\parallel$	3.03 ± 0.03	3.03 ± 0.05	3.01 ± 0.08	3.03 ± 0.08
$d_\perp$	3.05 ± 0.01	3.05 ± 0.04	3.02 ± 0.06	3.04 ± 0.06

$d_\parallel$ than for $d_\perp$. A similar situation arises at the O sublattice, with identical mean values of $d_\parallel$ and $d_\perp$, but larger dispersions reflecting the additional deformation of the sublattice. In turn, this causes significant variations of the Fe-O bond lengths, d(Fe-O), as reflected in the first column of Table III. However, the d(Fe-O) do not seem to follow any pattern with respect to the lattice or the magnetic order. The noticeable distortion of the FeO lattice is closely linked to the competition between the different superexchange paths. The magnetic order of the system is known to be dominated by the exchange interactions between second nearest neighbors (J_{2nn}), due to frustration of the first nearest neighbors interactions (J_{1nn}) [7]. Oppositely, the rhombohedral distortion of the unit cell is caused by spin-phonon couplings governed by the J_{1nn} [8]. The additional deformation of the O sublattice seems to be a mechanism to preserve maximization of the J_{2nn} under the presence of the magnetically induced phonon splitting.

IV. ISOLATED IRON VACANCY: $Fe_{0.97}O$

We have first considered the effect of creating one Fe vacancy in the cube of 64 atoms, which corresponds to $x = 0.03$. This situation is outside the experimental range of concentrations found for wüstite, as we reproduce from our estimations of E_c shown in Fig. 4. Its interest rather relies on the ability to isolate the features introduced by noninteracting vacancies. In Fig. 5 we show the total DOS of the supercell, together with the projections on the two different types of Fe that can be distinguished. The corresponding mean values and dispersions of the Bader charges and magnetic moments are in the second column of Table I. The emergence of Fe atoms that share more charge with O is evident. As mentioned in the Introduction, creation of an Fe vacancy is expected to induce a change of valence on two Fe cations, which should act as Fe^{3+}. We label them $Fe_B{}^{3+}$ by analogy to magnetite: in Fe_3O_4, Fe cations order in octahedral (B) and tetrahedral (A) sublattices, and at low temperatures a charge disproportionation at sublattice B leads to Fe atoms acting either with valence 3+ ($Q_B = 6.37$) or 2+ ($Q_B = 6.64$) [28,41]. Here, the $Fe_B{}^{3+}$ sites are among the first neighbors of the Fe vacancy, and belong to the same FM

TABLE III. Mean values and dispersions of the Fe-O bond lengths for the distinct types of Fe sites at the structures in Table I.

d(Fe-O), Å	FeO	$Fe_{0.97}O$	3 V_{Fe}	4:1
$Fe_B{}^{2+}$	2.15 ± 0.05	2.15 ± 0.07	2.14 ± 0.06	2.14 ± 0.07
$Fe_B{}^{3+}$		2.07 ± 0.05	2.05 ± 0.07	2.05 ± 0.06
$Fe_A{}^{3+}$				1.90 ± 0.02

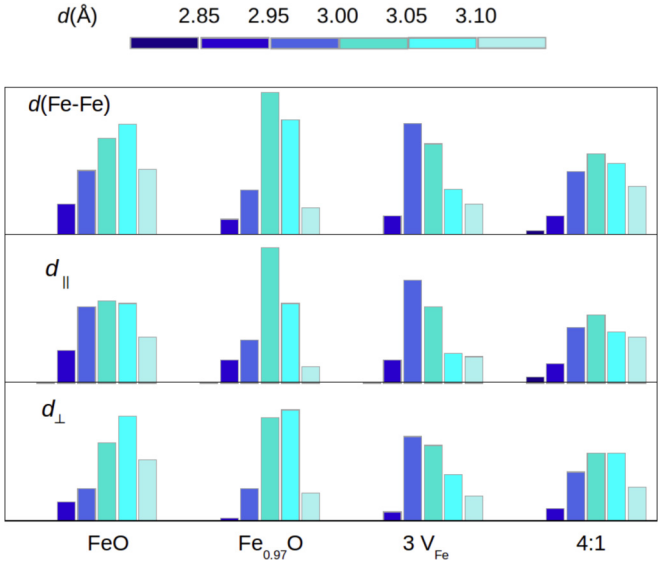

FIG. 3. (Color online) Histograms showing the distribution of values of d(Fe-Fe) at the Fe_B sublattice and its decomposition in $d_{\parallel}$ and $d_{\perp}$ for the structures in Table I. The vertical scale of the middle and bottom panels has been reduced by ∼30% with respect to the top panel.

layer [see Fig. 1(c)]. They introduce an incomplete charge compensation, leading to the slight reduction of the mean Q_B of O with respect to FeO. In general, the six O atoms, which are nearest neighbors (n.n.) to the vacancy show a lower charge than those farther from it, but the charge distribution is complex, and some O atoms far from the vacancy site hold similar low values of Q_B.

As evidenced in the table, accompanying the difference in Q_B there is an important enhancement of the magnetic moment at the Fe_B^{3+} sites, that also causes a slight increase of the induced O magnetization. This leads to the partial compensation of the AF coupling at the supercell, unbalanced by the V_{Fe}. However, a net magnetic moment of 2 μ_B yet remains, that together with the important reduction of the insulating gap to around 0.8 eV represent the main differences with respect to stoichiometric FeO. The new states at the gap

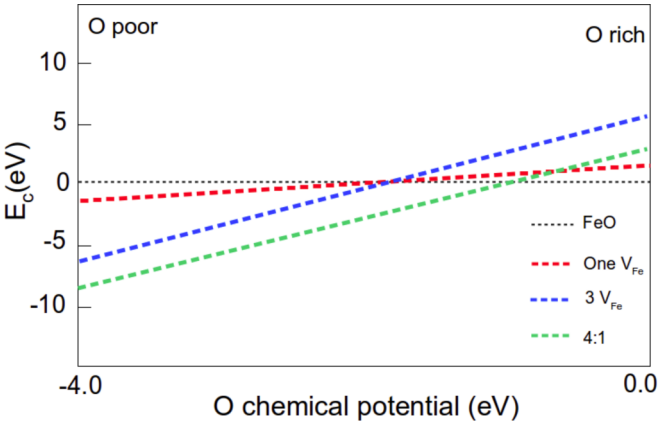

FIG. 4. (Color online) Energy cost of creating a defect at the different structures considered in Table I, as a function of μ_O.

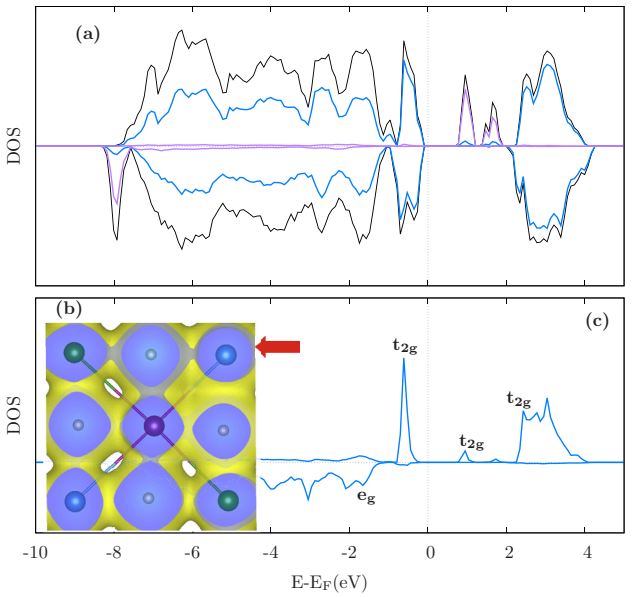

FIG. 5. (Color online) (a) Total DOS of $Fe_{0.97}O$ (black curve) with positive (negative) values corresponding to majority (minority) spins. The blue and purple curves are the projections on the Fe_B^{2+} and Fe_B^{3+} sites, respectively. (b) Charge density around an Fe_B^{3+} site, showing the accumulation of charge at certain Fe_B^{3+}-Fe_B^{2+} connecting lines. (c) DOS around the Fermi level of the Fe_B^{2+} pointed by an arrow in (b), showing the states directed along the CL that overlap with those of Fe_B^{3+}. The vertical scale is 10 times that in (a).

are precisely those coming from the Fe_B^{3+} states, that provide also the additional features at the bottom of the conduction band (CB). But the global electronic structure of the FeO lattice does not vary significantly, and most modifications are localized around the vacancy site.

The presence of the V_{Fe} introduces also changes in the structure. The second column of Table II summarizes the mean values of the interatomic distances between Fe neighbors, d(Fe-Fe), which together with the distribution of their values in Fig. 3 provide a measure of the rhombohedral distortion. As compared to stoichiometric FeO, there is a slight reduction of the cell volume and a tendency to shorten both $d_{\parallel}$ and $d_{\perp}$, better evidenced in Fig. 3. But the elongation along c is preserved for the low concentration of defects considered here. The relevant structural changes occur in the neighborhood of the vacancy. On one hand, they manifest in the d(Fe-O), compiled in the second column of Table III, which vary depending on the valence of Fe. The O atoms tend to approach the Fe_B^{3+} sites, while the average distance to Fe_B^{2+} remains similar to the stoichiometric case. The noticeable dispersion of the values reflects that a significant distortion of the fcc O sublattice as obtained for FeO still exists. On the other hand, there is an important rearrangement of the Fe positions in the vicinity of the V_{Fe}. Due to the fcc symmetry of the Fe sublattice, each vacancy has six Fe n.n. at the (111) plane, 3 n.n. above and 3 n.n. below. There is a tendency to fill the void created by the vacancy, which causes a slight shrinkage of the hexagon defined by its in-plane Fe neighbors [see Fig. 1(c)] and also of the triangles defined by its upper and lower n.n., which furthermore reduce their interlayer distances to the plane of

the vacancy. We find that the d(Fe-Fe) of stoichiometric FeO are gradually restored from the second n.n. to V_{Fe}. This was not observed in previous calculations [23], probably linked to an incomplete relaxation of the cubic symmetry.

Though the d(Fe-Fe) do not show the clear dependency with the Fe valence observed for d(Fe-O), some of the Fe_B^{2+} exhibit a singular relation to the neighboring Fe_B^{3+}, as indicated in the lower panels of Fig. 5. Figure 5(b) represents the three-dimensional real space distribution of the charge density in the (010) plane defined by an Fe_B^{3+} (central atom) and some of its Fe_B^{2+} neighbors (corner atoms). It is evident from the figure that there is a charge accumulation at one of the Fe_B^{3+}-Fe_B^{2+} connecting lines (CLs). The d(Fe-Fe) defined by this CL is considerably shortened to 2.88 Å, to be compared with values over 3 Å for the rest of Fe_B^{2+}-Fe_B^{3+} pairs in the figure. The charge accumulation at this short CL is also reflected in the DOS at Fig. 5(c), which shows the states of the corresponding Fe_B^{2+} overlapping those of Fe_B^{3+} at the FeO gap. Analysis of the orbital character of these states indicates that they are formed by t_{2g} orbitals lying along the CL. The combined presence of all these features is a signature of the short-range charge correlation units in magnetite [28], the trimerons, formed by groups of three neighboring Fe_B^{3+}-Fe_B^{2+}-Fe_B^{3+} sites with shortened interatomic distances and polaronic charge sharing [42,43]. We will discuss these aspects in more detail in the last section.

V. $Fe_{0.906}O$: ISOLATED VACANCIES

When three V_{Fe} are placed in the cube of 64 atoms, the maximum separation between them (around 6 Å) can be achieved under two magnetically inequivalent configurations. The situation is better visualized grouping all inequivalent Fe positions of the cube in two adjacent (111) planes of opposite spin orientation, as shown in Fig. 6. On the left side (case C1), two V_{Fe} lie on the same plane (blue) and the other on the adjacent one (green), resulting in one uncompensated Fe magnetic moment. On the right (case C2), all the vacancies lie on the same (111) plane, thus corresponding to removal of three Fe atoms with parallel spins. Surprisingly, in spite of the

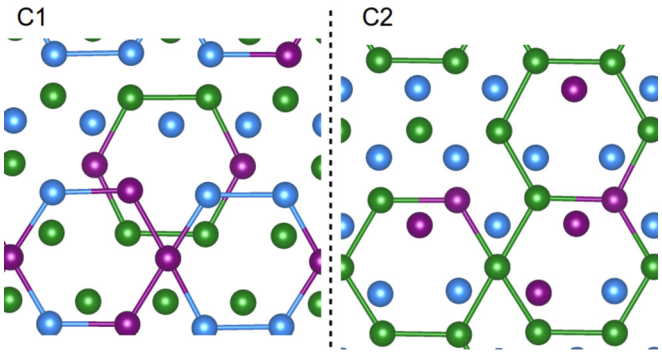

FIG. 6. (Color online) Top view of two adjacent Fe(111) planes of $Fe_{0.906}O$ with three isolated V_{Fe}, under configurations C1 (left) and C2 (right). The lines join the six in-plane n.n. of each V_{Fe}. The legend of Fig. 1 has been used, and the O sublattice has been omitted for clarity.

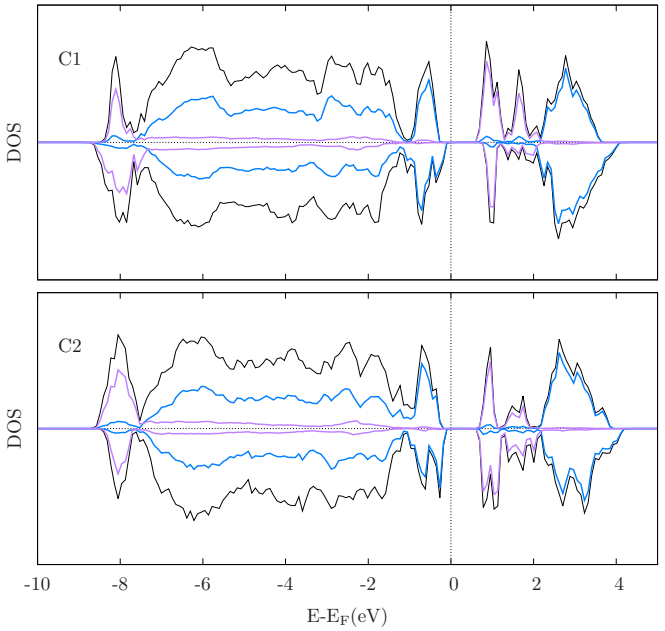

FIG. 7. (Color online) Same as Fig. 5(a) for the supercells modeling $Fe_{0.906}O$ with three isolated V_{Fe}. Top (bottom) panel corresponds to the C1 (C2) configuration.

large difference in their net magnetizations (2 μ_B for C1, 14 μ_B for C2), the total energies of both configurations are very close, the case C1 being favored by only 47 meV (less than 1 meV/atom). This tendency manifests also in the similarity of their global structural and electronic properties, and even though we will show that there are local differences between both cases, their resemblance is a hint of the non-interacting nature of the three V_{Fe}. This serves to put limits on the distance for Fe vacancies to interact. On the other hand, regarding Fig. 4, this composition is more stable than FeO at low O_2 pressures, and also more stable than $Fe_{0.97}O$ at the conditions where FeO is unstable, evidencing a tendency to cluster the defects.

The DOS of the supercells corresponding to C1 and C2 is shown in Fig. 7, together with the projections on the different types of cations. As occurred for one isolated vacancy, in both configurations two Fe per vacancy emerge with enhanced 3+ valence. Again they introduce new states at the bottom CB and at the insulating gap, reducing it to ∼0.5 eV. Comparing to the DOS of $Fe_{0.97}O$ in Fig. 5, the larger number of Fe_B^{3+} sites introduces additional states, that moreover appear at both spin orientations. In general all features of the DOS are broader, associated to the more defective structures.

The mean values of the charges and magnetic moments are summarized in the third column of Table I. They correspond to C1, but similar values are obtained for C2. As compared to $Fe_{0.97}O$, the increased number of V_{Fe} enhances the demand of charge from O, resulting in reduced Bader charges of both the Fe and O atoms. Also the Fe_B^{3+} are not only first neighbors to one V_{Fe}, but sometimes to two of them, which reflects in their reduced Q_B. As the Fe_B^{+3} atoms emerge to compensate the loss of charge donors introduced by the vacancies, not all of them lie on the same (111) plane of the closest V_{Fe}. Their enhanced magnetic moments thus reinforce the spin imbalance, an effect more pronounced in C2: while in C1 there is an equal number

of Fe_B^{3+} sites with each spin orientation, in C2 two Fe_B^{3+} are in the plane of the V_{Fe}, and four in the adjacent one. This combined with the small relative energy difference between C1 and C2 supports the interpretation of magnetic measurements, which assign to the defects local ferrimagnetic areas that are disordered with respect to each other and also with respect to the overall AF order [11,44].

In the third column of Tables II and III we show the mean values of the d(Fe-Fe) and d(Fe-O) for configuration C1. Again these global values, together with the unit cell vectors and cell volume, are very similar in C1 and C2. The volume contraction with respect to FeO is three times that found for $Fe_{0.97}O$, corresponding to a cubic lattice parameter of 4.26 Å. The average values of d(Fe-O) are also slightly shorter than for $Fe_{0.97}O$, reflecting the large demand of charge from O due to the increased number of V_{Fe}. Furthermore, there is a weakening of the rhombohedral distortion, in agreement with the experimental evidence [6,11]. This is better seen in the distribution of values of d(Fe-Fe) in Fig. 3, very similar for $d_{\parallel}$ and $d_{\perp}$. The large number of vacancies and the tendency of the Fe atoms to fill their voids shifts all distances to shorter values. Another important effect is that some pairs of Fe_B^{3+} are now first neighbors, inducing an accumulation of the valence charge in the interstitial region between them. This tends to inhibit the polaronic charge sharing between Fe_B^{3+}-Fe_B^{2+} pairs of shortened d(Fe-Fe) observed in the dilute limit $x = 0.03$. Regarding Fig. 7, here there are still Fe_B^{2+} states that overlap those of Fe_B^{3+} at the FeO gap. They are always linked to values of d(Fe-Fe) below 2.97 Å and to the existence of orbital order along the corresponding CL. However, no charge accumulation occurs at the interstitial region between Fe_B^{2+} and Fe_B^{3+}. The additional requirement for polaronic charge sharing is the shortening of the Fe_B^{2+}-Fe_B^{3+} interatomic distance below 2.89 Å, that is strongly suppressed by the accumulation of close Fe_B^{3+} sites.

In summary, the high concentration of V_{Fe} in $Fe_{0.906}O$ starts to break the homogeneity of the FeO matrix. Though each vacancy only modifies the local area surrounding it, and the interaction between vacancies is weak, the structure of FeO cannot accommodate such a large number of defects without altering its properties. This has important consequences for the charge distribution.

VI. $Fe_{0.906}O$: 4:1 CLUSTERS

The composition $Fe_{0.906}O$ can also be achieved by grouping the V_{Fe} in defect clusters. The most compact one is the 4:1 cluster, where we introduce an interstitial Fe at a tetrahedral coordination site, Fe_A, and surround it by four V_{Fe}. As one of the vacancy sites at the octahedral Fe sublattice is balanced by the creation of Fe_A, the stoichiometry corresponds to the effective introduction of three V_{Fe}, similarly to the case studied above. The 4:1 cluster is expected to be the most stable configuration for moderate values of x [27], and actually we obtain that it lowers the energy by 22 meV/atom as compared to the supercell with three isolated V_{Fe}. In turn, this extends the range of stability of defective $Fe_{1-x}O$ over FeO to higher O pressures, as shown in Fig. 4.

Figure 8 represents the 4:1 cluster embedded in our supercell, together with a top view of the (111) Fe layers around Fe_A, identifying the vacancy sites. It is evident from the figure that three out of the four V_{Fe} are first n.n. lying on the same (111) plane.

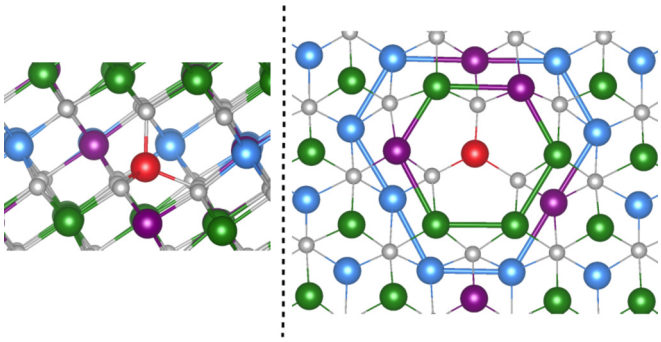

FIG. 8. (Color online) Side view along c (left) and top view (right) of $Fe_{0.906}O$ around a 4:1 cluster, following the legend in Fig. 1. On the right, only two adjacent (111) Fe layers are shown, and the Fe_A atom lies between them. The thick lines join the in-plane n.n. to the vacancy site.

Since the spin of Fe_A can be parallel or antiparallel to the layer with more vacancies, two magnetic configurations can be envisaged, with a very different uncompensated magnetization. As occurred for three isolated V_{Fe}, the corresponding ground states show similar global properties except for a very different net magnetic moment, of either 4 μ_B or 14 μ_B. The relative energy difference between both configurations is considerably higher than between C1 and C2, but still it is only moderate, of 5 meV/atom, and favors the situation with the lower magnetization. In fact most differences are similar to those discussed for C1 and C2, so in the following we will just describe the features of the most stable case.

The resulting DOS of the supercell and the projections on the different Fe sites are shown in Fig. 9, while the mean values of the Q_B and magnetic moments are summarized in the last column of Table I. The charge defect introduced by the three effective V_{Fe} would require six octahedral Fe_B^{3+} atoms. However, as Fe_A also acts with 3+ valence, only five Fe_B^{3+} atoms emerge. All of them are first n.n. to two V_{Fe} simultaneously, and they are also among the closest octahedral Fe neighbors of Fe_A, as shown in Fig. 8. The tetrahedral atom introduces additional states at the bottom conduction and valence bands, which overlap the contribution from Fe_B^{3+}, and

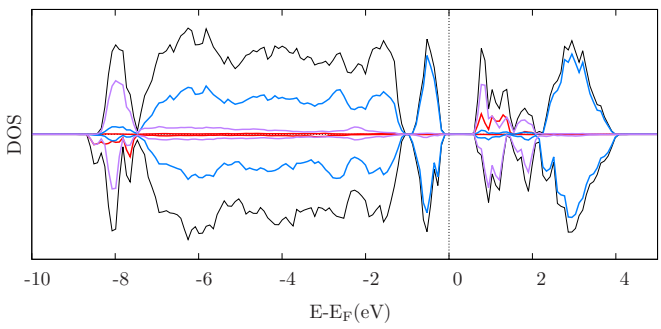

FIG. 9. (Color online) Same as Fig. 5(a) for the supercell modeling 4:1 clusters in $Fe_{0.906}O$. The red curve is the projection on the tetrahedral Fe_A^{3+} atom.

the resulting gap is ∼0.6 eV. Compared to cases C1 or C2, the distinct features corresponding to each type of Fe site in the DOS are better resolved, which evidences a higher degree of order in the structure. For example, the peaks associated to the t_{2g} and e_g states of Fe_B^{2+} at the top VB do not overlap, similarly to stoichiometric FeO, and opposite to all previous defect structures considered above. The higher localization of the defects also has consequences in the distribution of the O charges, which are lower (around 7.18) for the atoms bonded to Fe_A, and higher far from the defect, where they reach values similar to stoichiometric FeO. The result is that the mean Q_B at the O sublattice is enhanced over the configuration corresponding to three isolated V_{Fe}. This effectiveness of the 4:1 cluster to globally compensate the loss of charge introduced by the V_{Fe} seems to be at the origin of its higher stability.

The magnetic moments of Fe_B^{3+} and Fe_A^{3+} show less differences than their Q_B, and the induced magnetization at the O sublattice is similar for all distributions of V_{Fe} in $Fe_{0.906}O$. On the other hand, the formation of the clusters leads to the inhomogeneous distribution of the magnetic moments, with a higher magnetization in the region around the defects. This is in excellent agreement with previous experiments [45], where high magnetization and low temperature coercivity have been linked to the presence of large clusters based on stacking spinel-like defects.

The mean values and dispersions of d(Fe-Fe) and d(Fe-O) are summarized in the last columns of Tables II and III. The d(Fe-O) for the octahedral Fe sites do not differ substantially from the case corresponding to three isolated V_{Fe}, but there is an important shortening of the bond lengths corresponding to Fe_A. The values are close to those found at the tetrahedral sublattice in magnetite [28]. Oppositely, important differences can be found in the d(Fe-Fe) depending on the arrangement of the V_{Fe}. As evidenced in Fig. 3, the range of interatomic distances is wider in the presence of the 4:1 cluster, and their distribution closer to stoichiometric FeO than for any other defect structure in the figure. The largest differences to the stoichiometric case come from the increased similitude between $d_{\parallel}$ and $d_{\perp}$, and from the global shortening of the d(Fe-Fe), including the emergence of particularly low values below 2.85 Å. On one hand, this reflects the volume contraction to fill the voids left by the vacancies. On the other, the decrease of the magnetically induced rhombohedral distortion upon decrease of the Fe content, in good agreement with the experimental evidence. But in general, the FeO matrix tends to recover its structure far from the V_{Fe}, while the defect cluster introduces larger local modifications than the isolated vacancies. Furthermore, the shortest d(Fe-Fe) are signatures of the emergence of local polaronic charge distributions, as will be demonstrated in the next section.

VII. CHARGE DENSITY DISTRIBUTION. COMPARISON TO Fe_3O_4.

Magnetite, Fe_3O_4, is one of the stable forms of binary Fe oxides. It is a material of interest for magnetic applications, due to its unique properties of large magnetization, high magnetic ordering temperature, and half metallicity. Furthermore, at $T_V = 120$ K it undergoes a largely studied metal-insulator transition, the Verwey transition [41], where the interplay between structure and charge order (CO) is still under debate [46,47]. At ambient conditions the crystal structure is the cubic inverse spinel, that below T_V transforms into a large monoclinic unit cell accompanied by a drop of the conductivity and the emergence of CO at the octahedral Fe sublattice. Understanding the features of the CO in Fe_3O_4 has proved to be a complex task [48–51], and the survivance of short-range correlations above T_V linked to the long-range CO has been recently demonstrated [43]. The local order generated by the 4:1 clusters in $Fe_{1-x}O$ is a basic building block for the development of a spinel-like structure similar to that of magnetite. Moreover, the local properties around the defect are very similar to those of Fe_3O_4. Here we will explore how these similarities manifest also in the charge distribution, converting $Fe_{1-x}O$ in a unique material to understand the features of the CO of magnetite.

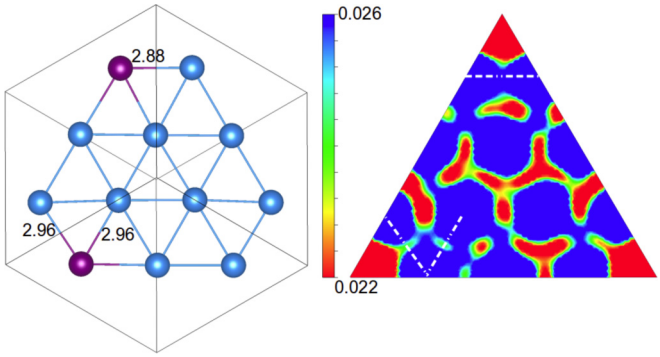

FIG. 10. (Color online) Two-dimensional slice of the charge density at the (111) plane containing the V_{Fe} in $Fe_{0.97}O$ (right), showing on the left the reference atomic positions. Representative interatomic distances (in Å) between Fe^{2+}-Fe^{3+} pairs are provided, and the corresponding CLs indicated by the dashed lines on the CD plot.

In Sec. IV we showed that a polaronic charge distribution reminiscent of Fe_3O_4 already emerges in the dilute limit represented by $Fe_{0.97}O$. Figure 5(b) identifies the existence of charge accumulation along certain shortened CLs between Fe_B^{2+}-Fe_B^{3+} neighbors. An alternative view of this effect is provided in Fig. 10, where a two-dimensional cut of the charge density (CD) at the (111) plane containing the vacancy is presented. In order to have a reference of the atomic centers, a sketch of the corresponding atomic positions is also shown, with vacancies lying at the corners of the triangle. The full CD spans a range between 1.285 $e/Å^3$ and 0.001 $e/Å^3$, while the range of interest for interatomic charge modulations at the (111) Fe planes is much reduced, as indicated by the color scale of the figure [52]. The maximum CD corresponds to the tails of the core charge, which decay very fast away from the atomic centers toward the interstitial regions. Usually there is a depression of the CD at the middle of the CL between Fe neighbors. As shown by the dashed lines in the figure, it tends to be less pronounced around the Fe_B^{3+} sites, and disappears only at the shortened Fe_B^{3+}-Fe_B^{2+} CLs corresponding to a d(Fe-Fe) = 2.88 Å, formed by overlapping t_{2g} Fe_B^{2+} and Fe_B^{3+} states directed along the CL.

The similitude to magnetite can be appreciated in Fig. 11, that shows the distribution of trimerons in a $P2/c$ unit cell

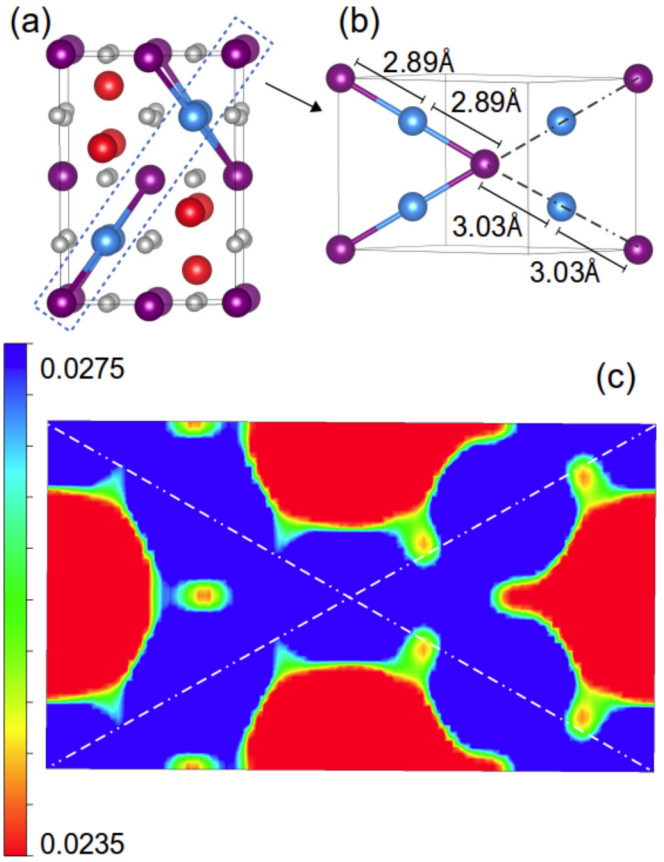

FIG. 11. (Color online) (a) Sketch of a $P2/c$ unit cell of Fe_3O_4 identifying the trimerons. The legend of Fig. 1 has been used. (b) Top view of a plane containing two trimerons. (c) Charge density at the plane in (b). The dashed lines follow the rows defined by the Fe_B atoms.

of Fe_3O_4 together with the CD at a plane containing them. Notice that in magnetite the Fe_B sublattice is ferromagnetic, and antiferromagnetically coupled to the Fe_A sublattice. As explained in Sec. IV, trimerons are linear chains of $Fe_B{}^{3+}$-$Fe_B{}^{2+}$-$Fe_B{}^{3+}$ n.n. with shortened interatomic distances (2.89 Å vs 3.03 Å) [28]. It is evident from the figure that the trimerons inhibit the depression of the CD at the middle of the CL between adjacent $Fe_B{}^{3+}$-$Fe_B{}^{2+}$ sites. The existence of two different Fe_A and Fe_B sublattices modifies the charge transfer with respect to wüstite, shifting the CD scale to slightly higher values.

In the case of three isolated V_{Fe} considered in Sec. V, the higher number of V_{Fe} makes the $Fe_B{}^{3+}$ sites to be sometimes n.n. Charge accumulation is always observed in the interstitial region between adjacent $Fe_B{}^{3+}$, as evidenced in Fig. 12. But these regions of large CD lack of any directionality in the orbital order and are not coupled to short d(Fe-Fe). Their existence, on the other hand, tends to inhibit the polaronic charge sharing between $Fe_B{}^{3+}$-$Fe_B{}^{2+}$ neighbors. In the supercell there is only one $Fe_B{}^{3+}$-$Fe_B{}^{2+}$ distance shortened to 2.89 Å where polarons are formed, indicated in Fig. 12. This proves the crucial role of the long-range distribution of $Fe_B{}^{3+}$ in the lattice for the emergence of polaronic charge sharing.

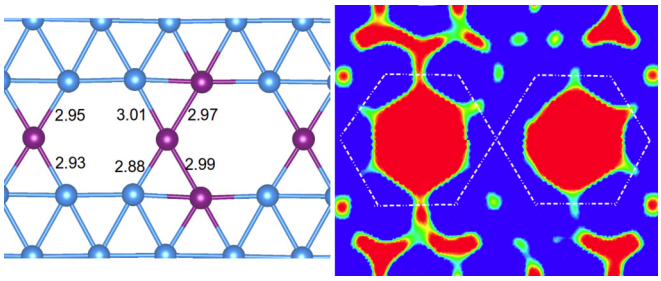

FIG. 12. (Color online) Same as Fig. 10 for case C1 of $Fe_{0.906}O$, at the (111) Fe plane where the shortest d(Fe-Fe) can be found.

The similitude to magnetite is recovered at 4:1 clusters, as shown in Fig. 13. The Fe_A atom promotes a distribution where no $Fe_B{}^{3+}$ are first n.n. On the other hand, it is almost coplanar along c to the plane with more V_{Fe}, filling the void created by them, and inhibiting the shrinkage of the irregular blue hexagon formed by the n.n. to the vacancies (see Fig. 8). Oppositely, at the plane with one vacancy the entire hexagon formed by the Fe_B around it shrinks, the shortest sides corresponding to $Fe_B{}^{3+}$-$Fe_B{}^{2+}$ CLs. These reduced d(Fe-Fe) are again accompanied by a polaronic charge distribution, as evidenced by the large CD (thick dashed lines in Fig. 13) and the orbital character of the corresponding $Fe_B{}^{2+}$ states. The fact that there are not any d(Fe-Fe) below the threshold 2.89 Å between adjacent layers of opposite spin polarization supports the close relation between these reduced interatomic distances and the formation of polarons.

As the distribution of the $Fe_B{}^{3+}$ sites is ultimately dictated by the O positions, there is a clear correlation between the emergence of polaronic charge sharing and the structure of

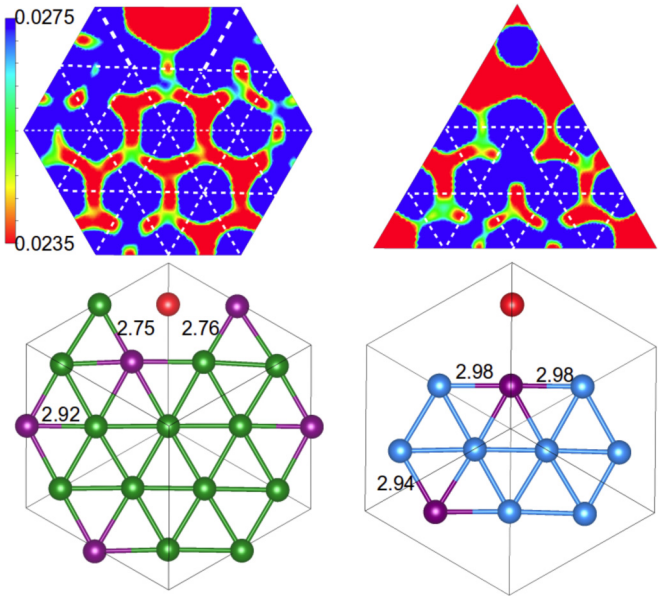

FIG. 13. (Color online) CD around a 4:1 defect cluster at the two different types of (111) planes in $Fe_{0.906}O$ (top). The reference atomic positions are indicated by dashed lines on top of the CD and at the lower panel, that also shows the projection of the Fe_A position. Representative values of the interatomic Fe^{2+}-Fe^{3+} distances are provided (in Å).

the O fcc sublattice. Also, the influence of the Fe_A sites in the distribution of the V_{Fe} has an important role to optimize the conditions for enhanced charge sharing. A distorted O sublattice with Fe atoms at tetrahedral sites also exists in magnetite [28], where furthermore there is more freedom to form polarons along any direction of the three-dimensional space due to the parallel alignment of the spins of the octahedral Fe atoms. In essence, this links unequivocally the long-range CO of magnetite to the short-range correlations, explaining the origin of diffuse scattering measurements that identified this connection and related the Fermi surface topology to the local CO [43].

VIII. CONCLUSIONS

$Fe_{1-x}O$ shows singular electronic properties that distinguish it from the rest of TMO and approach to the scenario defined by Fe_3O_4. The related physical phenomena emerge in reduced regions localized around the defects, converting $Fe_{1-x}O$ in a unique material to explore the complex interplay of lattice, charge, and spin degrees of freedom involved in the Verwey transition.

The creation of a Fe vacancy in FeO introduces charge disproportionation in the octahedral Fe sublattice, leading to two $Fe_B{}^{3+}$ at n.n. positions of the vacancy site. These $Fe_B{}^{3+}$ are characterized by enhanced magnetic moments and shorter bond lengths to O, as compared to the $Fe_B{}^{2+}$ of stoichiometric FeO. They are also responsible for the closing of the insulating gap from 2 eV to below 1 eV. Their ordering in the lattice is governed by the charge balance, causing uncompensated magnetic moments that create a net magnetization in $Fe_{1-x}O$.

In general, the Fe atoms tend to fill the voids created by the V_{Fe}, resulting in the contraction of the cell volume and the reduction of the rhombohedral distortion of FeO. Regardless of the distribution of the V_{Fe}, all alterations of the structural, electronic, and magnetic properties are localized around the defects, and far from them the features of the stoichiometric oxide tend to be recovered. Formation of compact defect clusters is clearly favored, probably linked to a more effective compensation of the global charge. However, the fast quenching process applied to obtain $Fe_{1-x}O$ at ambient conditions may produce samples where different configurations coexist. The most relevant features introduced by the 4:1 clusters are a high degree of overall order, due to the enhanced localization of the defects, a larger local magnetization, and the existence of more favorable conditions to form polarons.

In analogy to magnetite, the emergence of polaronic charge sharing is linked to the anomalous shortening of certain interatomic $Fe_B{}^{3+}$-$Fe_B{}^{2+}$ distances below a threshold value of 2.89 Å. The formation of polarons is conditioned by the distribution of the V_{Fe} and the $Fe_B{}^{3+}$ sites, which in turn depends on the internal structure of the O sublattice. This connects the local charge order to the long-range one, a phenomenon also observed in magnetite [43], thus allowing us to understand the origin of the relation between short-range correlations and charge order across the Verwey transition.

The influence of the magnetic interactions is at the same time complex and subtle. Together with the reduction of the magnetically induced rhombohedral distortion, the limited effect in the energy balance of local alterations of the magnetization around the defects supports a secondary role of the magnetism in the stability of the system. However, the existence of a distortion at the O fcc sublattice that requires the presence of magnetism is preserved when V_{Fe} are introduced. Furthermore, this distortion plays a crucial role in the emergence of polaronic charge distributions, which are favored under the most stable defect configurations. The importance of the magnetic interactions is higher when tetrahedral Fe_A sites are occupied, making plausible that the magnetic energy balance becomes crucial to determine the stability of large defect structures based on spinel-like clusters.

ACKNOWLEDGMENTS

This work has been financed by the Spanish Ministry of Economy and Competitiveness under Contract MAT2012-38045-C04-04. I.B. acknowledges financial support from the JAE program of the CSIC.

[1] J. Zaanen, G. A. Sawatzky, and J. W. Allen, Phys. Rev. Lett. **55**, 418 (1985).
[2] V. I. Anisimov, J. Zaanen, and O. K. Andersen, Phys. Rev. B **44**, 943 (1991).
[3] M. Däne, M. Lüders, A. Ernst, D. Ködderitzsch, W. M. Temmerman, and Z. Szotek, and W. Hergert, J. Phys.: Condens. Matter **21**, 045604 (2009).
[4] P. Thunstrom, I. Di Marco, and O. Eriksson, Phys. Rev. Lett. **109**, 186401 (2012).
[5] C. Rödl, F. Fuchs, J. Furthmüller, and F. Bechstedt, Phys. Rev. B **79**, 235114 (2009).
[6] B. T. Willis and H. P. Rooksby, Acta Crystallogr. **6**, 827 (1953).
[7] W. L. Roth, Phys. Rev. **110**, 1333 (1958).
[8] Ch. Kant, M. Schmidt, Z. Wang, F. Mayr, V. Tsurkan, J. Deisenhofer, and A. Loidl, Phys. Rev. Lett. **108**, 177203 (2012); W. Luo, P. Zhang, and M. L. Cohen, Solid State Commun. **142**, 504 (2007).
[9] N. C. Tombs and H. P. Rooksby, Nature (London) **165**, 442 (1950).
[10] C. G. Shull, W. A. Strauser, and E. O. Wollan, Phys. Rev. **83**, 333 (1951).
[11] H. Fjellvag, F. Gronvold, and S. Stolen, J. Solid State Chem. **124**, 52 (1996).
[12] P. J. Saines, M. G. Tucker, D. A. Keen, A. K. Cheetham, and A. L. Goodwin, Phys. Rev. B **88**, 134418 (2013).
[13] Y. Fei and H. K. Mao, Science **266**, 1678 (1994).
[14] K. Ohta, R. E. Cohen, K. Hirose, K. Haule, K. Shimizu, and Y. Ohishi, Phys. Rev. Lett. **108**, 026403 (2012).
[15] R. M. Hazen and R. Jeanloz, Rev. Geophys. Space GE **22**, 37 (1984).
[16] C. A. McCammon and L.-G. Liu, Phys. Chem. Miner. **10**, 106 (1984).
[17] D. V. Dimitrov, K. Unruh, G. C. Hadjipanayis, V. Papaefthymiou, and A. Simopoulos, J. Appl. Phys. **87**, 7022 (2000).

[18] F. Schrettle, Ch. Kant, P. Lunkenheimer, F. Mayr, J. Deisenhofer, and A. Loidl, Eur. Phys. J. B **85**, 164 (2012).
[19] D. P. Johnson, Solid State Commun. **7**, 1785 (1969).
[20] W. L. Roth, Acta Crystallogr. **13**, 140 (1960).
[21] A. K. Cheetham, Fender B. E. F., and R. I. Taylor, J. Phys. C **4**, 2160 (1971).
[22] M. R. Press and D. E. Ellis, Phys. Rev. B **35**, 4438 (1987).
[23] U. D. Wdowik, P. Piekarz, K. Parlinski, A. M. Oleś, and J. Korecki, Phys. Rev. B **87**, 121106(R) (2013).
[24] F. Koch and J. B. Cohen, Acta Crystallogr. Sect. B **25**, 275 (1969).
[25] C. R. A. Catlow and B. E. F. Fender, J. Phys. C **8**, 3267 (1975).
[26] C. Lebreton and L. W. Hobbs, Radiation Effects **74**, 227 (1983).
[27] L. Minervini and R. W. Grimes, J. Phys. Chem. Solids **60**, 235 (1999).
[28] I. Bernal-Villamil and S. Gallego, arXiv:1409.3012 [cond-mat.str-el] [J. Phys.: Condens. Matter (to be published)].
[29] G. Kresse and J. Hafner, Phys. Rev. B **47**, 558 (1993).
[30] G. Kresse and J. Furthmüller, Phys. Rev. B **54**, 11169 (1996).
[31] P. E. Blochl, Phys. Rev. B **50**, 17953 (1994).
[32] G. Kresse and D. Joubert, Phys. Rev. B **59**, 1758 (1999).
[33] J. P. Perdew, A. Ruzsinszky, G. I. Csonka, O. A. Vydrov, G. E. Scuseria, L. A. Constantin, X. Zhou, and K. Burke, Phys. Rev. Lett. **100**, 136406 (2008).
[34] S. L. Dudarev, G. A. Botton, S. Y. Savrasov, C. J. Humphreys, and A. P. Sutton, Phys. Rev. B **57**, 1505 (1998).
[35] A. Fujimori, N. Kimizuka, M. Taniguchi, and S. Suga, Phys. Rev. B **36**, 6691 (1987).
[36] I. Bernal-Villamil and S. Gallego (unpublished).
[37] C. G. Van de Walle and J. Neugebauer, Appl. Phys. Rev. **95**, 3851 (2004).
[38] K. Reuter and M. Scheffler, Phys. Rev. B **65**, 035406 (2001).
[39] C. Freysoldt, B. Grabowski, T. Hickel, J. Neugebauer, and G. Kresse, Rev. Mod. Phys. **86**, 253 (2014).
[40] I. I. Mazin and V. I. Anisimov, Phys. Rev. B **55**, 12822 (1997).
[41] E. J. W. Verwey, Nature (London) **144**, 327 (1939).
[42] M. S. Senn, J. P. Wright, and J. P. Attfield, Nature (London) **481**, 173 (2012).
[43] A. Bosak, D. Chernyshov, M. Hoesch, P. Piekarz, M. Le Tacon, M. Krisch, A. Kozlowski, A. M. Oleś, and K. Parlinski, Phys. Rev. X **4**, 011040 (2014).
[44] P. D. Battle and A. K. Cheetham, J. Phys. C: Solid State Phys. **12**, 337 (1979).
[45] D. V. Dimitrov, K. Unruh, G. C. Hadjipanayis, V. Papaefthymiou, and A. Simopoulos, Phys. Rev. B **59**, 14499 (1999).
[46] F. Walz, J. Phys.: Condens. Matter **14**, R285 (2002).
[47] J. García and G. Subías, J. Phys.: Condens. Matter **16**, R145 (2004).
[48] I. Leonov, A. N. Yaresko, V. N. Antonov, M. A. Korotin, and V. I. Anisimov, Phys. Rev. Lett. **93**, 146404 (2004).
[49] P. Piekarz, K. Parlinski, and A. M. Oleś, Phys. Rev. B **76**, 165124 (2007).
[50] J. García, G. Subías, J. Herrero-Martín, J. Blasco, V. Cuartero, M. C. Sánchez, C. Mazzoli, and F. Yakhou, Phys. Rev. Lett. **102**, 176405 (2009).
[51] S.-C. Weng, Y.-R. Lee, C.-G. Chen, C.-H. Chu, Y.-L. Soo, and S.-L. Chang, Phys. Rev. Lett. **108**, 146404 (2012).
[52] See Supplemental Material at http://link.aps.org/supplemental/10.1103/PhysRevB.90.195126 for a description of the full range charge density.